Dalton Transactions

Raman spectroscopic study of anhydrous and hydrous REE phosphates, oxides, and hydroxides

Journal:	*Dalton Transactions*
Manuscript ID	DT-ART-04-2024-001086.R1
Article Type:	Paper
Date Submitted by the Author:	10-May-2024

Complete List of Authors:	Hurtig, Nicole; New Mexico Institute of Mining and Technology, Earth and Environmental Science; New Mexico Tech Gysi, Alexander; New Mexico Institute of Mining and Technology, Earth and Environmental Science; New Mexico Bureau of Geology & Mineral Resources, New Mexico Institute of Mining and Technology Smith-Schmitz, Sarah; New Mexico Bureau of Geology & Mineral Resources, New Mexico Institute of Mining and Technology Harlov, Daniel; Deutsches Geoforschungszentrum Potsdam; China University of Geosciences, Faculty of Earth Resources; University of Johannesburg - Auckland Park Kingsway Campus, Department of Geology

Raman spectroscopic study of anhydrous and hydrous REE phosphates, oxides, and hydroxides

Nicole C. Hurtig[1*], Alexander P. Gysi[1,2], Sarah E. Smith-Schmitz[2] and Daniel Harlov[3,4.5]

[1] Dept. of Earth and Environmental Sciences, New Mexico Institute of Mining and Technology, 801 Leroy Place, 87801 Socorro

[2] New Mexico Bureau of Geology and Mineral Resources, New Mexico Institute of Mining and Technology, 801 Leroy Place, 87801 Socorro

[3] Deutsches GeoForschungsZentrum GFZ, Telegrafenberg, 14473 Potsdam, Germany

[4] Faculty of Earth Resources, China University of Geosciences, Wuhan 430074, China

[5] Department of Geology, University of Johannesburg P.O. Box 524, Auckland Park, 2006

South Africa

* corresponding author: nicole.hurtig@nmt.edu

Keywords: Raman spectroscopy, rare earth elements, phosphates, oxides, hydroxides, photoluminescence, solid solutions

Abstract

Rare earth elements (REE) include the lanthanides (La – Lu), Y, and Sc which are critical elements for the green energy transition. The REE show a decrease in ionic radii with increased atomic numbers, which results in a so-called lanthanide contraction systematically affecting crystal structures and mineral properties. Here we present a compilation of reference Raman spectra of ten REE sesquioxides (A-, B- and C-type), five REE hydroxides, eight xenotime-structured REE phosphate endmembers and two solid solutions, seven monazite-structured REE phosphate endmembers and two solid solutions and seven rhabdophane endmembers with up to five $Ce_{1-x}LREE_x$ rhabdophane solid solutions (LREE = La – Gd). Raman mode assignment is based on a detailed literature review summarizing existing analytical work and theoretical calculations and

systematic trends observed in this study by analyzing different REE-bearing solids. The wavenumbers of the main REE-O Raman band systematically increase with decreasing ionic radii forming discrete linear trends within isostructural mineral groups, that can be used to estimate the REE-O mode in other solids with known REE-O coordination numbers. Photoluminescence using 266 nm, 532 nm and 633 nm excitation laser wavelengths for REE-bearing oxides, hydroxides, anhydrous and hydrous phosphates is also presented providing a new framework for identifying REE-phases in phosphate-bearing natural mineral deposits.

Introduction

Rare earth elements (REE) are critical elements for the green energy transition with uses in wind turbines, electric vehicles, catalytic converters and solar panels [1–3]. In addition to the green technologies, REE are also important for other high technology and industry sectors including ceramics, metallurgy, magnets, phosphors and glasses [2]. The group of REE includes 16 lanthanides (La – Lu), Yttrium (Y) and Scandium (Sc) and can generally be subdivided into the light (L)REE which include La to Gd and the heavy (H)REE, which include Tb – Lu plus Y which is commonly considered as part of the HREE group [3–5]. Rare earth elements can be extracted from a range of ore deposits which include peralkaline-alkaline igneous complexes, carbonatites, iron-oxide apatite, placers, ion-absorption clay and phosphorite deposits [5]. Common REE-bearing minerals include monazite, xenotime, rhabdophane, bastnaesite and other fluorocarbonates and minerals such as eudialyte and other zirconosilicates [5]. Oxides and hydroxides are comparatively rare in natural ore deposits, where minerals such as pyrochlore may contain REE. However, they are important products during processing, extraction and concentration of REE [1]. Rare earth elements bearing phosphates have very low solubilities and are therefore an excellent host for immobilizing actinides with applications to radioactive waste disposal [6,7].

Raman spectroscopy is a powerful non-destructive analytical tool, that can provide micrometer-scale spatial resolution, and high-precision chemical and structural information on compounds with very little sample preparation [8–13]. As such Raman spectroscopy finds broad applications in mineral characterization for various REE deposits [14,15] and in material sciences to understand chemical and physical properties of REE compounds with applications to high technologies [16–18]. Rare earth sesquioxides (REE_2O_3) occur as three isostructural groups including

A-type hexagonal, B-type monoclinic and C-type bixbyite cubic, and their Raman modes have been extensively studied using theoretical calculations using the group theory and Raman spectroscopy. In the A-type hexagonal structure La, Pr and Nd oxides were previously measured [19–23] and in the B-type monoclinic structure Nd, Eu, Gd and Sc oxides have been studied [24–27]. In the C-type cubic structure, Pr, Nd, Sm, Eu, Gd, Tb-Lu, Y and Sc endmembers as well as Dy-Tm, Dy-Y and Ho-Y solid solutions were previously studied [9,24,25,28–37]. Hydroxides have been less studied with a few key studies summarizing La, Pr and Nd hydroxides [38], Nd hydroxide [39] and Nd-Gd, Tb and Dy hydroxides [40].

Orthophosphates occur in two isostructural groups comprising the tetragonal xenotime group which incorporates the HREE and the monoclinic monazite group which incorporates the LREE. All xenotime structured endmembers, including Tb-Lu, Gd, Y and Sc were previously characterized using Raman spectroscopy [10,41–47]. Solid solutions with the xenotime structure that were studied include Er-Yb [48], Gd-Dy [16] and more complex natural xenotime compositions [15]. Similarly, all La – Gd monazite structured endmembers [41,42,49,50] and the La-Eu solid solution [51] were characterized using Raman spectroscopy. The hydrated phosphate, rhabdophane, has been less studied with a few reference data available in the literature for the La, Ce, Nd and Gd endmembers [14,42,52,53].

While previous work on REE solids commonly describes their most prominent Raman modes, peak center positions may vary considerably between different studies and even between theoretical predictions using the group theory and measurements using different laser excitation wavelengths. This is a result of the interchangeability of the lanthanides in the respective mineral structures studied, leading to gradual peak center shifts within isostructural mineral groups. This becomes particularly relevant for mineral characterization of naturally occurring more complex solid solution compositions. In this study, we provide systematic reference tables for all Raman modes that were consistently measured in more than one study, more than three endmembers and more than one laser excitation wavelength. The synthetic REE minerals studied include: i) La, Nd, Sm, Eu, Dy, Ho, Er, Yb, Lu and Y sesquioxides (A, B and C-type); ii) La, Nd, Sm, Dy and Y hydroxides; and iii) Tb – Lu and Y xenotime, La – Gd monazite and La – Gd rhabdophane. We also present new data for Y-Dy and Y-Er 50-50 xenotime solid solutions, Ce-La and Ce-Nd 50-50 monazite solid solutions and data for rhabdophane solid solutions ($Ce_{1-x}LREE_x$; for LREE = La –

Gd). The reference files are available for download in the supplementary materials. This compilation provides an important framework for future studies investigating the systematics of lanthanide-bearing solids and naturally occurring complex REE-bearing minerals.

Methods and Materials

Sesquioxide powders (Alfa Aesar, 99.99% REO) were kept in a desiccator and dehydrated in an oven before measurement or use in REE hydroxide synthesis experiments. Rare earth element hydroxides and hydrated phosphates were synthesized at the New Mexico Bureau of Geology and Mineral Resources. The $REE(OH)_3$ powders were prepared using a hydrothermal method modified from Diakonov et al. [54]. A mixture of pure sesquioxide powders and Milli-Q water (18.2 MΩ·cm) were added to a 45 mL Teflon-lined Parr 4744 reactor and heated to 250°C for up to 21 days in a muffle furnace. After quenching, the REE hydroxide powders were collected, dried in a low temperature oven, and stored in a desiccator. Rhabdophane powders were synthesized by mixing ~2 ml of pure (or mixed for solid solutions) REE-bearing solutions, prepared by dissolving solid REE nitrates (Alfa Aesar, 99.99–99.999 % purity) into Milli-Q water, with ~100 ml of phosphate-bearing solutions (~40 mmol/kg P), which were prepared by dissolving solid $NH_4H_2PO_4$ (Acros Organics Chemicals, 99.999 % purity, trace metal basis) into Milli-Q water. The stirred mixed solutions resulted in instantaneous precipitation of rhabdophane solids which were allowed to equilibrate at ambient temperature for 30 min. The solids were subsequently separated from these solutions through a 0.45 μm membrane filter and oven-dried overnight at 60-75°C.

Monazite and xenotime, anhydrous phosphate single crystals consisting of a series of mixed compositions, were synthesized using techniques outlined in Cherniak et al. [55] at the GeoForschungsZentrum in Potsdam. A $REEPO_4$ powder (submicron grain size) was precipitated by mixing a REE nitrate solution with an ammonium dihydrogen phosphate solution (1:1 molar amounts). After the precipitate settled, the excess fluid was poured off and the precipitate allowed to dry. The ground powders were dry mixed with a Pb-free $NaCO_3$–MoO_3 flux ($75NaCO_3$:$25MoO_3$:$2REEPO_4$ molar ratio) in a 50:1 molar ration, placed in a Pt crucible with a cover and gradually heated in open air to 1375°C over a period of 4 h. The crucible was left at 1375°C for 15 h, and then slowly cooled to 870°C at 3°C/h over 6–7 days. The flux and embedded $REEPO_4$ crystals were then boiled in successive beakers of distilled H_2O until the crystals were

totally freed from the flux such that the flux could be poured off, leaving the completely clear, inclusion-free crystals behind.

Synthetic REE hydroxides and rhabdophane powders were analyzed using a Panalytical X-Pert Pro diffractometer and Cu-Kα radiation with scanning 2 angles or 5-70° and 0.02° step size. The samples were dry pressed and mounted on amorphous silica plates with randomly oriented crystals. The compositions and purity of these solid powders were verified using a Hitachi 224S-3200N scanning electron microscope equipped with a Thermo Fisher Noran System 6 energy dispersive spectrometer. Samples were mounted on carbon tape and carbon coated and analyzed using an acceleration voltage of 15 kV. Several points were measured across multiple grains for each endmember and solid solution compositions. The analyzed rhabdophane solid solutions are homogeneous and display variations within less than 1 % of their average compositions.

Compositions of the REE phosphate solid solutions ($Ce_{0.47}Nd_{0.53}PO_4$, $Ce_{0.46}La_{0.54}PO_4$, $Y_{0.53}Dy_{0.47}PO_4$, and $Y_{0.49}Er_{0.50}PO_4$) were determined using a Cameca SX-100 electron microprobe at New Mexico Bureau of Geology and Mineral Resources. The analyses were conducted using a 15 kV acceleration voltage, a beam current of 40 nA and a beam size of 10 μm. The elements analyzed, spectrometer crystals and counting times used include La (LLIF, 40 s), Ce (LLIF, 20 s), Nd (LLIF, 40 s), Y (TAP, 50 s), Er (LLIF, 40 s), Dy (LLIF, 40 s) and P (PET, 20 s). Detection limits based on repeated standard analysis are 670 ppm for La, 1500 ppm for Ce, 1400 ppm for Nd, 700 ppm for Y, 790 ppm for Er, 1800 ppm for Dy and 450 ppm for P.

Raman spectroscopy was performed on a Horiba LabRAM HR Evolution confocal microscope equipped with a 532 nm excitation Nd:YAG laser and a 266 nm excitation air cooled diode-pumped solid state (DPSS) UV laser. On the 532 nm excitation laser, analyses of the solids were performed using a 50x LWD objective (NA =0.5; WD = 10.6 mm) and 1800 grooves/mm grating with a spectral resolution of 0.2 cm^{-1}. Water peaks of rhabdophane were collected using the 600 grooves/mm grating combined with the 50x LWD objective with a spectral resolution of 1.5 cm^{-1}. On the 266 nm laser, analyses of the solids were performed using a 10x LUVB objective (NA =0.24; WD = 15 mm) and 2400 grooves/mm grating with a spectral resolution of 2 cm^{-1}. The instrument was calibrated using a first-order Si line at 520.7 cm^{-1} (silicon wafer) and an in-line standard reference objective (SP-RCO, Horiba, polystyrene) at 1000 cm^{-1} on the 532 nm excitation line and using a first-order C line in diamond at 1332 cm^{-1} for the 266 nm excitation line.

Instrument calibration was performed before analyses and after analyses, both analyses were within the expected uncertainty for the respective methods. Rhabdophane water peaks were also measured using a Horiba-Jobin Yvon Aramis Raman spectrometer equipped with a 633 nm-emitting HeNe laser and a 600 grooves/mm grating with a spectral resolution of 2 cm^{-1}.

Raman data were exported as text files and data reduction was performed using Fityk 1.3.1 [56]. All spectra were normalized and then corrected for background subtraction using a polynomial function and peaks were de-convoluted using Gaussian and/or Lorentzian functions based on best fit. Reference files for all solids presented in this study and Fityk files for deconvolution of spectra and fitting can be found in the supplementary materials. Measurements of Raman modes in this study are summarized in Tables 1-9 and Figures 1-6, with Figure 7 providing an overview of photoluminescence. Raman mode assignment is compiled from a literature review and is provided in the electronic supplementary information (Tables S1-S2).

Results and Discussion

Oxides and Hydroxides

A series of sesquioxide powders (La, Nd, Sm, Eu, Dy, Ho, Er, Yb, Lu and Y) were measured in this study using two laser excitation wavelengths (532 nm and 266 nm). Sesquioxides occur in three different crystallographic structures at ambient temperature, which comprise the A-type hexagonal structure for La – Nd, the B-type monoclinic structure for middle REE (Eu to Gd) and the C-type bixbyite structure for Sm – Lu including Sc and Y [57–59]. The A-type hexagonal structure belongs to the space group P-3m1 where trivalent REE ions are coordinated 7-fold with oxygen atoms [57]. The B-type monoclinic structure belongs to the C2/m space group and shows 6-fold and 7-fold coordinated trivalent REE ions hosted in two different crystallographic sites [57]. The C-type bixbyite structure belongs to the Ia-3 space group, which comprises a fluorite-type cubic lattice with ¼ of the oxygens sites vacant resulting in 6-fold coordinated trivalent REE cations located in the C_2 and the C_{3i} crystallographic sites [29,36,57,60,61].

Raman active modes for the A-type hexagonal structure (La_2O_3 and Nd_2O_3) were predicted to form four modes, i.e. $2A_{1g} + 2E_g$ [19–23,58]. The most prominent peak associated with A_{1g}, the stretching vibration of the REE-O polyhedron is reported at 407 ± 3, 413 and 435 ± 7 cm^{-1} for

La_2O_3, Pr_2O_3 and Nd_2O_3, respectively [19–21,23,32]. The literature values correspond to the measured peaks in this study, i.e., 405 ± 2 and 430 ± 2 cm^{-1} for La_2O_3 and Nd_2O_3 (Table 1; Fig. 1a). The A_{1g} peak is broad and slightly asymmetric indicating the band overlaps with another peak reported at 410 – 480 cm^{-1} [19–21,23,32]. This study shows a peak overlap at 364 cm^{-1} in La_2O_3 using the 532 nm excitation laser, which is not observed on the 266 nm laser and an overlap at ~432 and 476 cm^{-1} in Nd_2O_3 using 532 nm and 266 nm excitation lasers, respectively. Differences in Raman mode activation using different excitation laser wavelengths and/or polarizers indicate that several peaks indeed overlap between 400 – 450 cm^{-1} for hexagonal sesquioxides, which may explain the different shapes of the main peak and slight peak center shifts. The highest peak is very narrow and can be observed at ~104 cm^{-1} and corresponds to either E_g of the asymmetric bending vibration [23] or A_{1g} of the symmetric bending mode for the REE-O polyhedron [21]. There are two smaller peaks at 64 cm^{-1} and at ~184 – 190 cm^{-1} that are observed in both oxides and a few other peaks that were observed between 100 – 900 cm^{-1}, however not consistently in both oxides and using both laser excitation wavelengths (Table 1 data this study; Table S2 reference values).

The monoclinic B-type structure has been observed for Sc_2O_3 at high pressures [26], for Eu_2O_2 [62], Gd_2O_3 [25] and Sm_2O_3 at ambient conditions. Theoretical predictions indicate 21 Raman active modes using group theory, i.e. $14A_g + 7B_g$ [27], of which 16 are typically measured [24–26,32,62,63]. The Raman spectra for B-type oxides is more complicated compared to A-type oxides, which only have one major peak. In B-type oxides, there are several overlapping peaks with peak heights varying considerably between the 266 and 532 nm excitation lasers due to different Raman mode activation. The main peak group (i.e., A_g^8, B_g^4, B_g^5, A_g^9 and A_g^{10}) comprises 4 – 5 overlapping peaks similar in height and full widths half maxima (FWHM) occurring at 340 ± 3, 372 ± 1, 397 ± 1, 419 ± 2 and 460 ± 1 cm^{-1} in Sm_2O_3 (Table 2; Fig. 1b). This peak group shows four peaks at 296, 363, 387 and 472 cm^{-1} for Nd_2O_3 [24] and five peaks at 373, 393, 411, 423 and 463 cm^{-1} for Eu_2O_3 [62] and at 386, 417, 430, 442 and 483 cm^{-1} in Gd_2O_3 [25]. At lower wavenumbers, peaks at 81, 96, 109, ~119, ~169, 174, ~208, ~246, 256 and 281 cm^{-1} were measured in Sm_2O_3, Eu_2O_3 and Gd_2O_3; all of which indicate very little peak shifts with increasing ionic radii. Finally, the peak at 568 ± 1 cm^{-1} measured in Sm_2O_3 shifts to 577 cm^{-1} in Eu_2O_2 [62] but has not been described in other B-type oxides in previous studies. Additional peaks observed using the 532 nm laser for Sm_2O_3 may represent photoluminescence, which is described further below and were not observed during measurements using the 266 nm excitation laser (Fig. 1b).

Most of the other sesquioxides (Eu – Lu, Sc and Y) occur in the C-type bixbyite structure with 22 predicted Raman active modes, i.e., $4A_g + 4E_g + 14F_g$ [28,29,36,58]. Typically, there is only one strong band between 320 and 420 cm^{-1} with several minor peaks resulting in 1 to 16 measured modes reported in previous studies [9,24,28–31,33,35–37,58,64]. In this study, 17 modes were determined in Eu, Dy, Ho, Er, Yb, Lu and Y oxides using the 266 and 532 nm laser excitation wavelengths (Table 3). The most prominent mode corresponds to the symmetric stretching vibration of REE-O, which is commonly assigned to a combination of $F_g + A_g$ [29,31,36], and was measured at 335 ± 3 cm^{-1} for Eu_2O_3, 371 ± 1 cm^{-1} for Dy_2O_3, 375 ± 1 cm^{-1} for Ho_2O_3, 376 ± 1.5 cm^{-1} for Y_2O_3, 377 ± 1 cm^{-1} for Er_2O_3, 360 ± 1 cm^{-1} for Yb_2O_3 and 391 ± 1 cm^{-1} for Lu_2O_3 (Fig. 1c). This mode is generally broad and has a shoulder at lower and/or higher wavenumbers. At high wavenumbers, there are two consistent Raman modes that occur as significant peaks increasing from 425 to 497 cm^{-1} and from 566 to 611 cm^{-1} between Eu_2O_3 and Lu_2O_3. At low wavenumbers, a clear peak occurs at 314 – 345 cm^{-1} (Eu to Lu), two large narrow peaks consistently occur at ~96 and 120 cm^{-1}, and two smaller peaks occur at ~135 and 145 cm^{-1}. Raman peak centers below 200 cm^{-1} do not shift and remain constant between Eu and Lu indicating that these modes correspond to lattice vibrations.

The main stretching vibrational mode for oxides depends on the crystal system and the coordination number of the trivalent REE ion in the REE-O polyhedron (Fig. 1d). This mode occurs at 407 – 430 cm^{-1} for A-type La_2O_3 to Nd_2O_3, where the REE ion is 7-fold coordinated in the REE-O polyhedron. In B-type Nd_2O_3 to Gd_2O_3 oxides, we identified A_g^8 and A_g^9 as the peaks corresponding to the main stretching vibrational modes of 6- and 7-fold coordinated REE-O at 296 – 386 and 387 – 442 cm^{-1}, respectively. In C-type bixbyite structures (Pr_2O_3 – Lu_2O_3 including Sc_2O_3 and Y_2O_3) REE are 6-fold coordinated and the main peak mode occurs at 322 – 419 cm^{-1}. Within each structural group the peaks are shifted to higher wavenumbers with decreasing ion radii [65] or increasing atomic numbers (Fig. 1d). Exceptions to this trend are the symmetric stretching vibrations, i.e., F_g+A_g, in C-type Eu_2O_3 and Yb_2O_3, which show lower wavenumbers compared to the trend (Fig. 1d). In comparison, hydroxides have 9-fold coordinated REE-O polyhedra, which show a separate trend at higher wavenumbers, i.e., E_{1g} 450 – 507 cm^{-1} for La to Y, compared to 6- and 7-fold coordinated REE-O polyhedra in the oxides.

Rare earth hydroxides with the general formula $REE(OH)_3$ (REE = La to Lu) are hexagonal and belong to the $P6_3/m$ space group [38,66]. The trivalent REE ions are coordinated with nine oxygen

atoms with two different REE-O and three different O-O bond distances [66]. Previous studies indicate four to six Raman active modes are predicted and/or measured, i.e., $1 - 3A_{1g} + 2E_{1g} + 2E_{2g}$ [38–40]. The three most prominent peaks (P1 – P3) increase from $La(OH)_3$ to $Y(OH)_3$ and indicate measured values of 281 – 314 cm^{-1} for A_g i.e., peak 1, 340 – 399 cm^{-1} for A_g or E_{2g} i.e., peak 2, and 450 – 507 cm^{-1} for E_{1g} i.e., peak 3 (Table 4; Fig. 2a,b), which is consistent with previous works [19,24,38–40,67,68]. In Dy and Y hydroxide, the middle modes at 395 and 399 cm^{-1} display a shoulder at ~406 cm^{-1}, which is not observed in the LREE hydroxides. The peak heights of the main modes systematically change with decreasing ionic radii with peak 1 and 2 showing a constant ratio and peak 3 showing increasing peak heights (Fig. 2c). In addition to the three main modes described above, we also measured a narrow mode at 139 cm^{-1}, a mode shifting from 228 to 262 cm^{-1} and a double peak shifting from 630 and 650 cm^{-1} to 700 and 745 cm^{-1} with decreasing lanthanide ionic radii. A minor peak group is observed at ~750, 785 and 819 cm^{-1}, which could only be detected using the 266 nm excitation laser (Table 4). The peak at 1070 cm^{-1} in $La(OH)_3$ shifts to higher wavenumbers with decreasing ionic radii to 1084 cm^{-1} measured in $Y(OH)_3$. In this study, we also identified 17 small modes between 44 and 130 cm^{-1}, which likely correspond to lattice vibrational modes, because they remain at their respective wavenumber and do not shift with increasing lanthanide atomic numbers and decreasing ionic radii (Fig. 2a). Finally, the OH vibrational mode (E_{1g} libration of OH dipole) occurs at ~3600 cm^{-1} and shifts toward lower wavenumbers in the light REE (La to Sm) from 3602 to 3596 cm^{-1} and shows a shoulder shifting to higher wavenumbers from ~3608 to 3618 cm^{-1} in Sm to Y hydroxides.

Phosphates

Xenotime is an anhydrous phosphate, with the general formula of $HREEPO_4$ (HREE = Y, Tb-Lu) and a tetragonal crystal structure of the $I4_1/amd$ space group [69]. The PO_4 tetrahedron alternates with 8-fold coordinated trivalent REE-O polyhedra forming chains [69]. Theoretical simulations indicate 12 Raman active vibrational bands corresponding to five external modes with symmetries: at $2B_{1g} + 3E_g$ and seven internal modes with symmetries at $2A_{1g} + 2B_{1g} + B_{2g} + 2E_g$ [41,43,45–47,70,71]. Eleven modes can be measured consistently in xenotime endmembers presented in this study (Table 5), which reproduce reported values from the literature [10,15,16,41,43–48].

The highest peak corresponds to symmetrical stretching vibrations (ν_1) of the PO_4 tetrahedron corresponding to A_{1g}, which was measured at 994 ± 0.5 cm^{-1} for $TbPO_4$ and systematically shifts to higher wavenumbers with decreasing lanthanide radii reaching 1010 ± 0.5 cm^{-1} for $LuPO_4$ (Fig. 3a). The asymmetric stretching vibrational band (ν_3) i.e., B_{1g}, occurs at 1049 cm^{-1} for $TbPO_4$ and increases to 1068 cm^{-1} for $LuPO_4$. The symmetric bending vibrational mode (ν_2), i.e., A_{1g} for the PO_4 tetrahedron correspond to 484 cm^{-1} for $TbPO_4$ and 487 cm^{-1} for $LuPO_4$, showing a minor peak shift of <3 cm^{-1} between Tb and Lu. Asymmetric bending modes (ν_4) i.e., B_g occurs at 650 cm^{-1} for $TbPO_4$ and shift towards higher wavenumbers at 664 cm^{-1} for $LuPO_4$. The mode predicted at ~260 cm^{-1} (E_g(T) see [41]) or 266 cm^{-1} (B_{gv2} see [70]), was not observed in this study. Three lattice vibration modes were also measured and occur between 100 and 200 cm^{-1}.

Peak center positions systematically shift to higher wavenumbers with decreasing ionic radii in the xenotime endmembers (Fig. 4). The three peaks related to stretching vibrations v_1 and v_3 of the PO_4 tetrahedron in xenotime increase by 16 – 19 cm^{-1} between Tb and Lu (Fig. 4a). Similarly, the v_4 asymmetric bending vibration also increases by 14 cm^{-1}, whereas the peak assigned to the v_2 symmetric bending vibration of the PO_4 tetrahedron only increases by 3 cm^{-1} (Fig. 4b). The peak assigned to E_g(R) at 292 – 304 cm^{-1} shows an increase of 13 cm^{-1} between the Tb and Lu xenotime endmembers and peaks assigned to lattice vibrations remain constant with decreasing ionic radii (Fig. 4c). Based on the linear correlations for 6-, 7- and 9-fold coordinated REE-O polyhedra in oxides and hydroxides we estimate that the REE-O mode should occur between 470 and 497 cm^{-1} in xenotime which has 8-fold coordinated REE-O polyhedra. The closest Raman mode measured in this range is at 484 to 486 cm^{-1} currently assigned to ν_2-PO_4. The peak center positions for YPO_4 plot slightly above the linear trend between Tb and Lu. The measured Raman modes in YPO_4 correspond to values of 1000 ± 2 cm^{-1} for ν_1, 1057 ± 1 cm^{-1} for ν_3, 658 ± 2 cm^{-1} for ν_2 and 482 ± 1 cm^{-1} for ν_4 measured in previous studies [10,41,45,47]. The Y-Dy and Y-Er 50-50 solid solutions plot on a linear trend between their respective endmembers and deviate from the linear trends between Tb and Lu xenotime endmembers (Fig. 4).

Monazite is an anhydrous phosphate ($LREEPO_4$), which includes the light rare earth elements (LREE = La-Gd) and has a monoclinic crystal structure. Monazite belongs to the $P2_1/n$ space group [69,72,73] with alternating chains of PO_4 tetrahedra and 9-fold coordinated trivalent REE-O polyhedra. Theoretical simulations show 36 Raman active modes with 18 internal i.e., $9A_g + 9B_g$

and 18 external modes i.e., $6A_gT + 3A_gR + 6B_gT + 3B_gR$ [41,50]. Here we identified 27 Raman modes that are consistently measured by more than one study, more than one laser excitation line and in more than three REE endmembers (Table 6). Previous studies report between 17 – 24 peaks [41,42,49–51].

The highest Raman peak is measured at 966 ± 0.5 cm^{-1} for $LaPO_4$ and systematically shifts towards higher wavenumbers at 988 ± 0.5 cm^{-1} and 986 ± 0.5 cm^{-1} for the Eu and Gd monazite endmembers (Fig. 3b). This peak is commonly associated with the symmetrical stretching vibration (ν_1) of the PO_4 tetrahedron [41,49,51]. In the most recent publication by Errandonea et al. [50], $B_g(\nu_1)$ and $A_g(\nu_1)$ are predicted at 923 and 930 cm^{-1} for La, respectively, whereas the peak at 968 cm^{-1} (predicted at 959 cm^{-1}) is associated with $A_g(\nu_3)$. This assignment seems controversial because their largest peak occurs above 950 cm^{-1} in their figures, which is consistent with the ν_1 stretching modes in measured in our study and others [41,49,51]. The main PO_4 stretching and bending modes comprise the largest Raman peaks which are consistently detected in all of the REE monazite endmembers (Fig. 3b) and match well with previous studies [17,41,42,49,51,74–76].

Raman peaks for asymmetrical (ν_3) and symmetrical (ν_2) stretching modes and asymmetrical (ν_4) bending modes for the PO_4 tetrahedron linearly increase from La to Gd monazite endmembers from 1055 – 1072, 463 – 476 and 618 – 631 cm^{-1}, respectively (Fig. 4a-b). Similar to previous studies, the monazite-(Eu) endmember shows a positive and negative deviation from the linear trends for ν_1 and ν_2, respectively [17,41,49]. At frequencies above 300 cm^{-1}, peaks shift systematically by 1-4% or 8-22 cm^{-1} towards higher wavenumbers except for the peak at 537 cm^{-1}, which only increases by 0.5% or 2 cm^{-1} along the LREE series. Similarly to xenotime, we used the REE-O peak positions from the REE hydroxides to estimate the potential location for 9-fold coordinated REE-O polyhedra at 454 to 492 cm^{-1}. This range overlaps with the prominent Raman mode at 465 – 476 cm^{-1}, which is currently assigned to ν_2-PO_4. Lattice vibrations in monazite have been proposed to occur either below 450 [17,41,49], 420 [51,75,76] or 380 cm^{-1} [50]. The lattice vibrations (external Raman modes) at 88, 121 and 130 cm^{-1} only vary within 1 cm^{-1}, modes at 150 and 256 cm^{-1} increase systematically by up to 6% and modes at 100, 169, 218, 225 and 270 cm^{-1} increase systematically by up to 10% along decreasing ionic radii within the LREE series (Fig. 4c). The peak positions for the 50-50 Ce-La and Ce-Nd solid solutions plot linearity between their respective endmembers.

Rhabdophane is a hydrous phosphate mineral with the general formula $LREEPO_4 \cdot nH_2O$ (LREE = La-Gd, n = 0.667). The crystal structure has been investigated in detail for $SmPO_4 \cdot 0.667H_2O$ [77], $GdPO_4 \cdot 0.667H_2O$ [42] and $Ce_{1-x}Nd_xPO_4 \cdot 0.667H_2O$ [78] indicating a monoclinic crystal system in the C2 space group. The structure is defined by infinite channels formed by six chains of alternating REE-O and PO_4 polyhedra oriented along [101] [77]. The REE-O polyhedra can be 8- and 9-fold coordinated depending on which chain they are residing in [77]. One chain contains H_2O linked to REE-O polyhedra and PO_4 tetrahedra, whereas the second chain is free of water and contains linked REE-O and PO_4 tetrahedra [77]. Previous studies identified between 8 – 11 Raman peaks which were related to the vibrational modes of the PO_4 tetrahedron [18,42,53,78].

In this study we describe 20 measured Raman modes, which were measured in all rhabdophane endmembers (Table 7). The most prominent peak assigned to ν_1 of the PO_4 tetrahedron is deconvoluted with three sub-peaks, of which the main peak shifts from 973 cm^{-1} in rhabdophane-(La) to 992 cm^{-1} in rhabdophane-(Gd). The two ν_1-subpeaks at higher wavenumbers, correspond to 8- and 9-fold coordinated REE-PO_4 tetrahedrons, which systematically follow trends observed in xenotime endmembers for 8-fold coordinated REE and 9-fold coordinated REE ions in monazite endmembers. The smallest ν_1-subpeak, is the least systematic and shows larger deviations between different laser excitation wavelengths indicating that it may be affected by photoluminescence or have other structural implications. Symmetric and asymmetric stretching vibrations of rhabdophane solid solutions $Ce_{1-x}LREE_x$ (LREE = Pr, Nd, Eu, Gd) plot linearity between the endmembers (Fig. 5; Table 8). The asymmetric stretching vibrational mode ν_3 is at 1082 – 1106 cm^{-1} for La to Gd (Fig. 5a). The PO_4 bending vibrational modes ν_2 and ν_4 are at 467 – 470 and 623 – 632 cm^{-1}, respectively and lattice modes generally occur below 300 cm^{-1} and show no or only minor increases in wavenumbers with decreasing ionic radii along the LREE lanthanide series (Fig. 5c). Predicted Raman bands for the 8- and 9-fold coordinated REE-O polyhedra estimated based on the oxides and hydroxides are expected to occur at 418 – 464 and 454 – 492 cm^{-1}, respectively. Estimated Raman bands for 8-fold coordinated REE-O overlap with the measured mode at 410 – 458 cm^{-1}, and for 9-fold coordinated REE-O overlap with the measured mode at 467 – 470 cm^{-1}, which are both currently assigned to ν_2 of the PO_4 tetrahedron (Fig. 5c).

The water peak in rhabdophane is deconvoluted using three subpeaks (ν_{H2O} peak 1-3), which occur at ~3290, 3450 and 3586 cm^{-1} (Fig. 6; Table 9) corresponding to network water,

intermediate water and hydroxyl vibrational modes [79–81]. The water peak was measured using the 266, 532 and 633 nm excitation lasers because of laser induced photoluminescence interfering with the water mode in Nd-, Sm-, Eu- and Gd-bearing rhabdophane solid solutions and endmembers (Figs. 6a, b and 7b, c). The water peak intensity significantly decreases between La, Ce and Pr, which show a clear water band and Gd, which only shows a weak water band (Fig. 6a, b). The peak percentage for peak 1 to 3 for free water is ~ 69%, 18% and 13 %, which corresponds closely to the measured peak percentages of 74%, 20% and 6% for La, Ce and Pr rhabdophane endmembers and solid solutions using 532 nm and 633 nm excitation lasers (Fig. 6a, b). Peak 3 is more challenging to fit and often depends on the extent of background corrections applied, which vary significantly in Nd to Gd rhabdophane endmembers due to photoluminescence. Peak 3 shows a slight positive trend with decreasing ionic radii with a lot of scattering for rhabdophane-(Nd) to -(Gd). The area of the first peak (network water) systematically decreases and the area of the second peak (intermediate water) increases with decreasing ionic radii (Fig. 6c, d). Systematic changes in the water band have been previously related to changes in pore size of silica nano porous materials [80] and changes in the O-H, O-O and H-O-H bonded water and hydroxyl molecules in minerals [81], indicating a decrease in the crystallographic site for water molecules with decreasing ionic radii along the LREE lanthanide series in rhabdophane.

Photoluminescence

Laser induced photoluminescence is common in REE-bearing solids [9,17,18,27,82–85] and occurs due to the 4f electron configurations of REE^{3+} ions, which may result in narrow band widths similar to typical Raman modes [13,83,86]. Here prominent fluorescence was observed in Nd, Sm, Eu, Gd, Er and Ho solids when using the 532 nm excitation laser (Fig. 7) and in Ce, Nd, Sm, Eu and Gd rhabdophane endmembers and solid solutions using the 633 nm excitation laser (Fig. 6b). Similar photoluminescence bands have been assigned to minor and trace amounts of Nd^{3+}, Sm^{3+}, Eu^{3+}, Ho^{3+} and Er^{3+} in naturally occurring zircon, xenotime and monazite [83,86].

The Nd sesquioxides shows broad photoluminescence between 2000 – 2900 cm^{-1} and 3600 – 4500 cm^{-1}. The luminescence is shifted to lower wavenumbers in the Nd-hydroxide and occurs at 1500 – 2000 cm^{-1} and at ~3600 – 3800 cm^{-1} generally exhibiting narrower peaks compared to the Nd-oxide (Fig. 7a). Monazite-(Nd) and rhabdophane-(Nd) show broadly overlapping

fluorescence with that of the Nd-hydroxide. The fluorescence peaks between 3600 and 3800 cm^{-1} overlap with the water peak in rhabdophane and gradually increase in solid solutions between the Ce and Nd endmembers (Fig. 7b). Discrete photoluminescence peaks occur in the Sm-oxide, Sm-hydroxide, and monazite-(Sm) between 800 and 1200 cm^{-1}, which are of similar intensity and FHWM compared to the Raman modes in these solids. Broad fluorescence bands are observed between 1800 – 2300 cm^{-1} and 3200 – 3600 cm^{-1} in Sm-oxide, Sm-hydroxide, and monazite-(Sm) with discrete narrow peaks occurring in hydroxide and monazite (Fig. 7a). Rhabdophane-(Sm) shows three large peak groups at 1600 – 1900 cm^{-1}, 2400 – 2700 cm^{-1}, and 4300 – 4600 cm^{-1} and two smaller peak groups at ~1500 and ~3500 cm^{-1} overlapping with water Raman modes. In Ce-Sm rhabdophane solid solutions, five discrete photoluminescence bands modify the Raman active mode of the water molecule (Fig. 7c). The peak at ~3200 cm^{-1} occurs in Ce-rich solid solutions, but importantly is not observed in the Ce endmember, whereas the peak at ~3500 cm^{-1} becomes more pronounced in the Sm-rich solid solutions and its respective endmember, indicating that Ce-Sm solid solutions exhibit new optical properties that are different from their respective endmembers. Xenotime-(Eu) and rhabdophane-(Eu) show prominent photoluminescence between 1700 – 2100 cm^{-1}, 2400 – 2700 cm^{-1} and 4300 – 4600 cm^{-1} and a narrow peak at ~1550 cm^{-1} and 3400 cm^{-1} overlapping with the Raman modes of water in rhabdophane (Fig. 7d). The largest luminescence peak in monazite-(Eu) occurs at ~1700 cm^{-1} and at 4400 cm^{-1} in rhabdophane-(Eu). Photoluminescence in the Gd endmembers of monazite and rhabdophane are of much lower intensity compared to the Eu endmembers, with discrete peaks occurring at ~900, 1100, 1550, 1700 and 4200 cm^{-1} and peak groups at 1800 – 2100, 2200 – 3200, 3100 – 3500 and 4300 – 5400 cm^{-1} (Fig. 7d). Rhabdophane-(Gd) shows much broader luminescence peaks compared to monazite-(Gd), which is susceptible to 'bleaching' i.e., signal decrease after extended time of laser exposure. Significant laser-induced photoluminescence was observed in Ho- and Er-oxides and xenotime (Fig. 7e), which broadly overlap at ~ 500 – 800 cm^{-1} and 3100 – 4000 cm^{-1} in oxides and 300 – 700 cm^{-1} and 3200 – 3800 cm^{-1} in xenotime.

Conclusions

This compilation of Raman modes and photoluminescence peaks for the entire lanthanide series for oxides, hydroxides and phosphates provides a new framework for future research on REE

solids and interpretation of complex natural minerals. Systematic data collection and peak center shifts of the main Raman active modes provide the foundation for more consistent peak assignment and matching measured Raman spectra to theoretically predicted modes using the group theory. The REE-O vibrational mode shows distinctive linear trends for 6-, 7- and 9-fold coordinated REE ions which systematically shift to higher wavenumbers with decreasing ionic radii and increasing atomic numbers. Applying the observed trends for the REE-O modes from oxides and hydroxides to phosphates, REE-O mode locations can be estimated for monazite, xenotime and rhabdophane based on the REE coordination numbers in these solids. Peak centers for Raman modes systematically shift between the endmembers along the lanthanide contraction series including solid solutions, which plot linearly between their respective endmembers. The main stretching and bending vibrational modes of the PO_4 tetrahedron occur along linear trends with decreasing ionic radii for a given REE coordination number and are therefore predictable between different mineral structures. A few exceptions to this rule are the main Raman vibrational mode F_g+A_g of Yb_2O_2 at 360 cm^{-1}, which shows lower wavenumbers compared to the linear trend of the main REE-O band with decreasing ionic radii. Similarly, YPO_4 and Y-bearing xenotime solid solutions show higher wavenumber for ν_1-PO_4 and the lattice vibrations, than what would be expected based on the linear trends of the respective Raman modes with decreasing ionic radii. Deviation from these linear trends may indicate possible crystal structure distortion because of changes in REE ion radii sizes. Detailed characterization of photoluminescence patterns and reference spectra for the entire REE series in different solids may become an important tool for identification of naturally occurring REE-bearing mineral phases and could find applications in phosphate-bearing REE deposit characterization.

Acknowledgments

This research was significantly supported through the NSF/EAR-MRI #2117061, through which the confocal Raman microscope was purchased. This research is based upon work supported by the U.S. Department of Energy, Office of Science, Office of Basic Energy Sciences, Geosciences program under Award Number DE-SC0022269, specifically focusing on REE-O coordination chemistry. We thank Dr. Nikolai Kalugin for help with analyses using the 633 nm excitation laser wavelength and comments on the manuscript.

Author Contributions

NH, AG and SS analyzed solids using Raman spectroscopy, XRD and SEM and AG and DH synthesized minerals for this study. All authors contributed towards writing this manuscript. We thank two anonymous reviewers for their constructive feedback and comments.

Conflicts of interest

There are no conflicts to declare.

References

1 T. Dutta, K. H. Kim, M. Uchimiya, E. E. Kwon, B. H. Jeon, A. Deep and S. T. Yun, *Environ Res*, 2016, **150**, 182–190.

2 B. Zhou, Z. Li and C. Chen, *Minerals*, 2017, **7**, 203.

3 H. F. Leslie, M. Nordvig and S. Brink, *Critical Materials Strategy*, 2010.

4 N. G. Connelly, T. Damhus, R. M. Hartshorn and A. T. Hutton, *Nomenclature of inorganic chemistry: IUPAC Recommendations*, 2005.

5 K. R. Long, B. S. Van Gosen, N. K. Foley and D. Cordier, *Non-Renewable Resource Issues: Geoscientific and Societal Challenges*, 2012, 131–155.

6 E. Du Fou de Kerdaniel, N. Clavier, N. Dacheux, O. Terra and R. Podor, *Journal of Nuclear Materials*, 2007, **362**, 451–458.

7 N. Dacheux, N. Clavier and R. Podor, *American Mineralogist*, 2013, **98**, 833–847.

8 A. E. Maftei, A. Buzatu, G. Damian, N. Buzgar, H. G. Dill and A. I. Apopei, *Minerals*, 2020, **10**, 1–17.

9 J. C. Panitz, J. C. Mayor, B. Grob and W. Durisch, *J Alloys Compd*, 2000, **303–304**, 340–344.

10 W. P. Griffith, *Nature*, 1969, 224, 264–266.

11 A. Wang, J. Han, L. Guo, J. Yu and P. Zeng, *Appl Spectrosc*, 1994, **48**, 959–968.

12 G. Giridhar, R. R. K. N. Manepalli and G. Apparao, in *Spectroscopic Methods for Nanomaterials Characterization*, Elsevier Inc., 2017, **2**, 141–161.

13 G. Panczer, D. De Ligny, C. Mendoza, M. Gaft, A.-M. Seydoux-Guillaume and X. Wang, in *Raman spectroscopy applied to Earth sciences and cultural heritage*, eds. G. Ferraris, J. Dubessy, M.-C. Caumon and F. Rull, European Mineralogical Union, 2012, 61–82.

14 I. A. Zhukova, A. S. Stepanov, A. V. Korsakov and S. Y. Jiang, *Journal of Raman Spectroscopy*, 2022, **53**, 485–496.

15 E. Švecová, R. Čopjaková, Z. Losos, R. Škoda, L. Nasdala and J. Cícha, *Mineral Petrol*, 2016, **110**, 747–765.

16 M. A. Musselman, T. M. Wilkinson, B. Haberl and C. E. Packard, *Journal of the American Ceramic Society*, 2018, **101**, 2562–2570.

17 J. Heuser, A. A. Bukaemskiy, S. Neumeier, A. Neumann and D. Bosbach, *Progress in Nuclear Energy*, 2014, **72**, 149–155.

18 M. T. Colomer, J. Bartolomé, A. L. Ortiz and A. de Andrés, *Ceram Int*, 2017, **43**, 10840–10847.

19 D. L. Hoang, A. Dittmar, M. Schneider, A. Trunschke, H. Lieske, K. W. Brzezinkab and K. Witke, *Thermochim Acta*, 2003, **400**, 153–163.

20 M. Scheithauer, H. Knözinger and M. A. Vannice, *J Catal*, 1998, **178**, 701–705.

21 J. H. Denning and S. D. Ross, *Journal of Physics C: Solid State Physics*, 1972, **5**, 1123–1133.

22 J. Zarembowitch, J. Gouteron and A. M. Lejus, *Physica status solidi B*, 1979, **94**, 249–256.

23 S. I. Boldish and W. B. White, *Spectrochim Acta A*, 1979, **35**, 1235–1242.

24 J. Cui and G. A. Hope, *Journal of Spectroscopy*, 2015, **2015**, 1–8.

25 L. Laversenne, Y. Guyot, C. Goutaudier, M. T. Cohen-Adad and G. Boulon, *Opt Mater (Amst)*, 2001, **16**, 475–483.

26 D. Liu, W. Lei, Y. Li, Y. Ma, J. Hao, X. Chen, Y. Jin, D. Liu, S. Yu, Q. Cui and G. Zou, *Inorg Chem*, 2009, **48**, 8251–8256.

27 M. T. Candela, F. Aguado, A. Diego-Rucabado, J. A. González and R. Valiente, *J Alloys Compd*, 2022, **921**, 166043.

28 M. V. Abrashev, N. D. Todorov and J. Geshev, *J Appl Phys*, 2014, **116**, 103508.

29 N. D. Todorov, M. V. Abrashev, V. Marinova, M. Kadiyski, L. Dimowa and E. Faulques, *Phys Rev B Condens Matter Mater Phys*, 2013, **87**, 104301.

30 L. A. Tucker, F. J. Carney, P. McMillan, S. H. Lin and L. Eyring, *Appl Spectrosc*, 1984, **38**, 857–860.

31 G. Schaack and J. A. Koningstein, *J Opt Soc Am*, 1970, **60**, 1110.

32 J. Gouteron, D. Michel, A. M. Lejus and J. Zarembowitch, *J Solid State Chem*, 1981, **38**, 288–296.

33 M. W. Urban and B. C. Cornilsen, *Journal of Physics and Chemistry of Solids*, 1987, **48**, 475–479.

34 V. Grover, A. Banerji, P. Sengupta and A. K. Tyagi, *J Solid State Chem*, 2008, **181**, 1930–1935.

35 X. Fu, Y. Xu and J. Zhou, *J Mater Sci*, 2012, **47**, 1697–1701.

36 Y. Repelin, C. Proust, E. Husson and J. M. Beny, *J Solid State Chem*, 1995, **118**, 163–169.

37 A. A. Kaminskii, S. N. Bagaev, K. Ueda, K. Takaichi, J. Lu, A. Shirakawa, H. Yagi, T. Yanagitani, H. J. Eichler and H. Rhee, *Laser Phys Lett*, 2005, **2**, 30–35.

38 S. R. Sanivarapu, J. B. Lawrence and G. Sreedhar, *ACS Omega*, 2018, **3**, 6267–6278.

39 S. Arunachalam, B. Kirubasankar, V. Murugadoss, D. Vellasamy and S. Angaiah, *New Journal of Chemistry*, 2018, **42**, 2923–2932.

40 S. Liu, Y. Liu, Q. Mu, F. Zhang, H. Li and Y. Wang, *Appl Phys A Mater Sci Process*, 2013, **111**, 1229–1240.

41 G. M. Begun, G. W. Beall, L. A. Boatner and W. J. Gregor, *Journal of Raman Spectroscopy*, 1981, **11**, 273–278.

42 N. Clavier, A. Mesbah, S. Szenknect and N. Dacheux, *Spectrochim Acta A Mol Biomol Spectrosc*, 2018, **205**, 85–94.

43 E. Stavrou, A. Tatsi, E. Salpea, Y. C. Boulmetis, A. G. Kontos, Y. S. Raptis and C. Raptis, *J Phys Conf Ser*, 2008, **121**, 042016.

44 R. J. Elliott, R. T. Harley, W. Hayes and S. R. P. Smith, *Proceedings of the Royal Society of London*, 1972, **328**, 217–266.

45 M. Giarola, A. Sanson, A. Rahman, G. Mariotto, M. Bettinelli, A. Speghini and E. Cazzanelli, *Phys Rev B Condens Matter Mater Phys*, 2011, **83**, 1–8.

46 A. Tatsi, E. Stavrou, Y. C. Boulmetis, A. G. Kontos, Y. S. Raptis and C. Raptis, *Journal of Physics Condensed Matter*, 2008, **20**, 425216.

47 A. N. Lazarev, N. A. Mazhenov and A. P. Mirgorodskij, *Izv. Akad. Nauk SSSR, Neorg. Mater*, 1978, **14**, 2107–2118.

48 A. C. Strzelecki, M. Reece, X. Zhao, W. Yu, C. Benmore, Y. Ren, C. Alcorn, A. Migdisov, H. Xu and X. Guo, *ACS Earth Space Chem*, 2022, **6,** 5, 1375–1389.

49 E. N. Silva, A. P. Ayala, I. Guedes, C. W. A. Paschoal, R. L. Moreira, C. K. Loong and L. A. Boatner, *Opt Mater (Amst)*, 2006, **29**, 224–230.

50 D. Errandonea, O. Gomis, P. Rodriguez-Hernández, A. Munz, J. Ruiz-Fuertes, M. Gupta, S. N. Achary, A. Hirsch, F. J. Manjon, L. Peters, G. Roth, A. K. Tyagi and M. Bettinelli, *Journal of Physics Condensed Matter*, 2018, **30**, 065401.

51 T. Geisler, K. Popa and R. J. M. Konings, *Front Earth Sci (Lausanne)*, 2016, **4**, 64.

52 H. Liu, X. Zhao, Y. Teng, Y. Li, X. Zheng, S. Wang, L. Wu, P. K. Panda and R. Ahuja, *Journal of the American Ceramic Society*, 2022, **105**, 4974–4985.

53 S. Lucas, E. Champion, D. Bernache-Assollant and G. Leroy, *J Solid State Chem*, 2004, **177**, 1312–1320.

54 I. I. Diakonov, B. R. Tagirov and K. V. Ragnarsdottir, *ract*, 1998, **81**, 107–116.

55 D. J. Cherniak, J. Pyle and J. Rakovan, *American Mineralogist*, 2004, **89**, 1533–1539.

56 M. Wojdyr, *urn:issn:0021-8898*, 2010, **43**, 1126–1128.

57 S. C. Atkinson, University of Salford, 2013.

58 A. Ubaldini and M. M. Carnasciali, *J Alloys Compd*, 2008, **454**, 374–378.

59 B. J. Kennedy and M. Avdeev, *Solid State Sci*, 2011, **13**, 1701–1703.

60 L. Eyring, K. Gschneidner and G. Lander, *Handbook on the physics and chemistry of rare earths*, Elsevier Science B.V., Amsterdam, The Netherlands, 1st edn., 2001, vol. 32.

61 H. Kohlmann, *Zeitschrift für Naturforschung B*, 2019, **74**, 433–435.

62 M. T. Candela, F. Aguado, A. Diego-Rucabado, J. A. González and R. Valiente, *J Alloys Compd*, 2022, **921**, 166043.

63 M. T. Candela, F. Aguado, J. A. González and R. Valiente, *J Alloys Compd*, 2023, **967**, 1–11.

64 W. B. White and V. G. Keramidas, *Spectrochim Acta A*, 1972, **28**, 501–509.

65 R. D. Shannon, *Acta Crystallographica Section A*, 1976, **32**, 751–767.

66 G. W. Beall, W. O. Milligan and H. A. Wolcott, *Journal of Inorganic and Nuclear Chemistry*, 1977, **39**, 65–70.

67 Q. Mu and Y. Wang, *J Alloys Compd*, 2011, **509**, 2060–2065.

68 S. S. Chan and A. T. Bell, *J Catal*, 1984, **89**, 433–441.

69 Y. Ni, J. M. Hughes and A. N. Mariano, *American Mineralogist*, 1995, **80**, 21–26.

70 P. Dawson, M. M. Hargreave and G. R. Wilkinson, *Journal of Physics C: Solid State Physics*, 1971, **4**, 240–256.

71 P. C. Becker, N. Edelstein, G. M. Williams, J. J. Bucher, R. E. Russo, J. A. Koningstein, L. A. Boatner and M. M. Abraham, *Phys Rev B*, 1985, **31**, 8102–8110.

72 N. Clavier, R. Podor and N. Dacheux, *J Eur Ceram Soc*, 2011, **31**, 941–976.

73 R. C. L. Mooney, *J Chem Phys*, 1948, **16**, 1003.

74 A. Hirsch, P. Kegler, I. Alencar, J. Ruiz-Fuertes, A. Shelyug, L. Peters, C. Schreinemachers, A. Neumann, S. Neumeier, H. P. Liermann, A. Navrotsky and G. Roth, *J Solid State Chem*, 2017, **245**, 82–88.

75 T. Huang, J. S. Lee, J. Kung and C. M. Lin, *Solid State Commun*, 2010, **150**, 1845–1850.

76 N. Huittinen, Y. Arinicheva, P. M. Kowalski, V. L. Vinograd, S. Neumeier and D. Bosbach, *Journal of Nuclear Materials*, 2017, **486**, 148–157.

77 A. Mesbah, N. Clavier, E. Elkaim, C. Gausse, I. Ben Kacem, S. Szenknect and N. Dacheux, *Cryst Growth Des*, 2014, **14**, 5090–5098.

78 H. Liu, X. Zhao, Y. Teng, Y. Li, X. Zheng, S. Wang, L. Wu, P. K. Panda and R. Ahuja, *Journal of the American Ceramic Society*, 2022, **105**, 4974–4985.

79 Q. Sun, *Vib Spectrosc*, 2009, **51**, 213–217.

80 A. W. Knight, N. G. Kalugin, E. Coker and A. G. Ilgen, *Sci Rep*, 2019, **9**, 1–12.

81 B. Kolesov, *American Mineralogist*, 2006, **91**, 1355–1362.

82 H. Lösch, A. Hirsch, J. Holthausen, L. Peters, B. Xiao, S. Neumeier, M. Schmidt and N. Huittinen, *Front Chem*, 2019, **7**, 1–16.

83 C. Lenz, L. Nasdala, D. Talla, C. Hauzenberger, R. Seitz and U. Kolitsch, *Chem Geol*, 2015, **415**, 1–16.

84 Z. Zhao, J. Zuo and Z. Ding, *Journal of Rare Earths*, 2010, **28**, 254–257.

85 Q. G. Zeng, Z. J. Ding, B. F. Lei, Y. Q. Sheng and Z. M. Zhang, *High Press Res*, 2012, **32**, 412–418.

86 C. Lenz, D. Talla, K. Ruschel, R. Škoda, J. Götze and L. Nasdala, *Mineral Petrol*, 2013, **107**, 415–428.

Figures

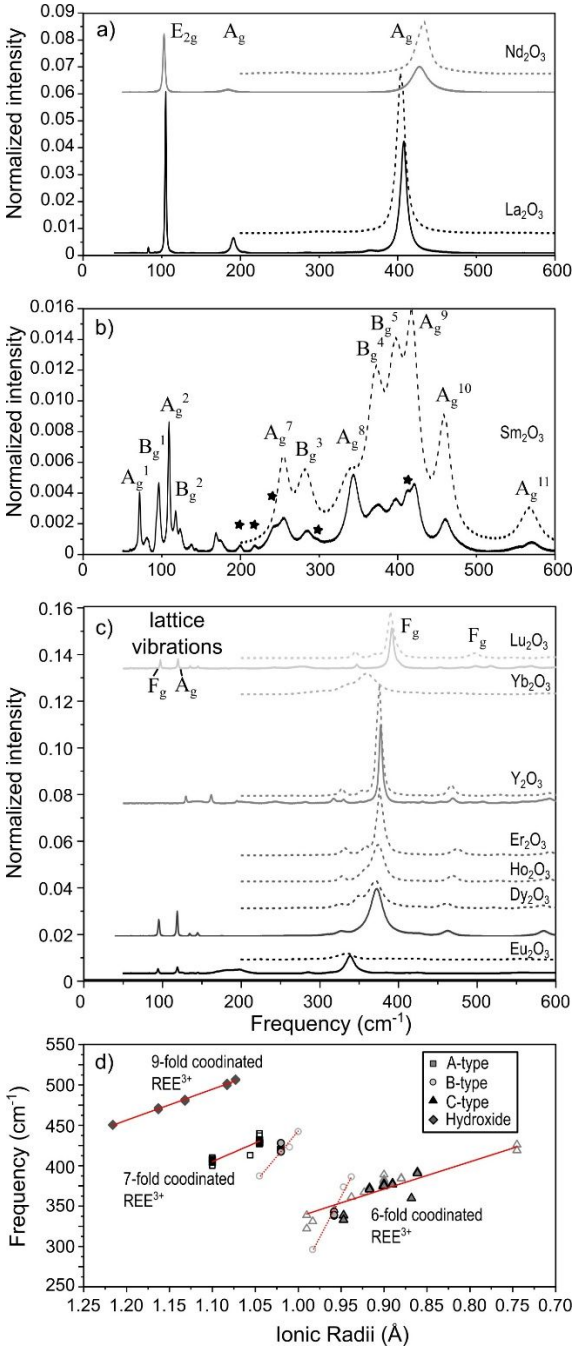

Figure 1: Raman spectra for of a) A-type hexagonal, b) B-type monoclinic, and c) C-type bixbyite structured sesquioxides using the 532 nm (solid lines) and 266 nm (dashed lines) excitation lasers. Black stars indicate extra peaks. (d) Main stretching vibrational modes for 7-fold and 6-fold coordinated REE-O in A-, B- and C-type structures as well as 9-fold coordinated REE-O in hydroxides, showing discrete trends with decreasing ionic radii for each isostructural mineral group (Shannon, 1970). Closed symbol = this study, open symbols = previous studies listed in the supplementary Tables S1-S2.

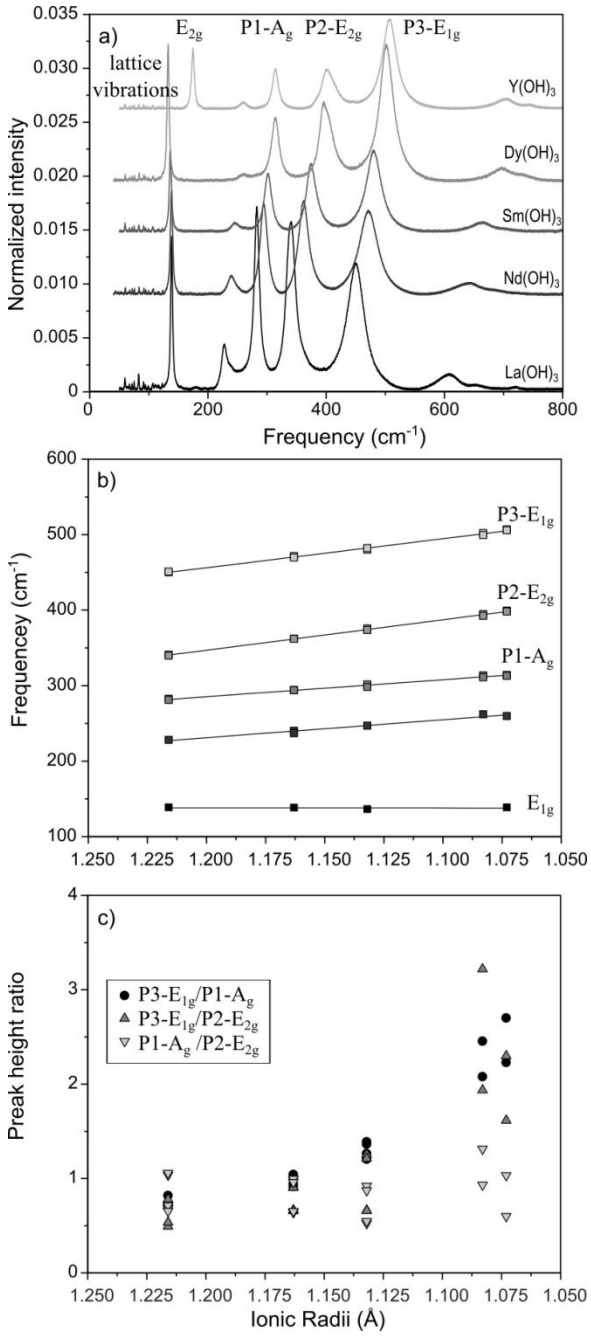

Figure 2: a) Raman spectra of REE hydroxides measured using the 532 nm excitation laser. b) Raman peak centers for the three main peaks (P1-P3) increase systematically with decreasing ionic radii, of these we identified P3 (E_{1g}) to represent the main stretching vibrational mode of 9-fold coordinated REE ions. c) Peak height ratios P3/P1 and P3/P2 increase exponentially with decreasing ionic radii and P1/P2 remain constant.

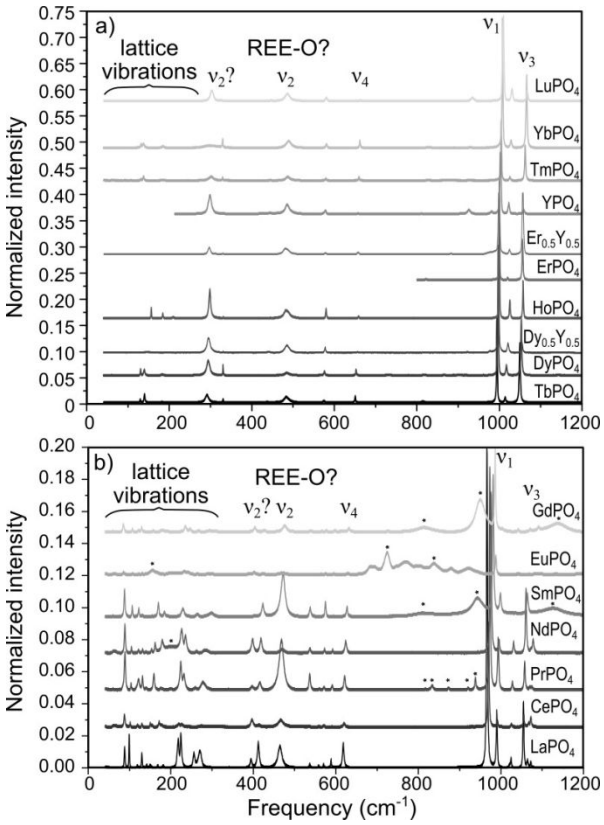

Figure 3: Raman spectra of (a) xenotime and (b) monazite showing the major vibrational modes $\nu_1 - \nu_4$ of the PO_4 tetrahedron and indicating the potential location of the major REE-O peak for 9- and 8-fold coordinated trivalent REE-O polyhedra based on observations from oxides and hydroxides (Figs. 1-2, Tables 1-4). Additional peaks most likely related to photoluminescence are marked with a star.

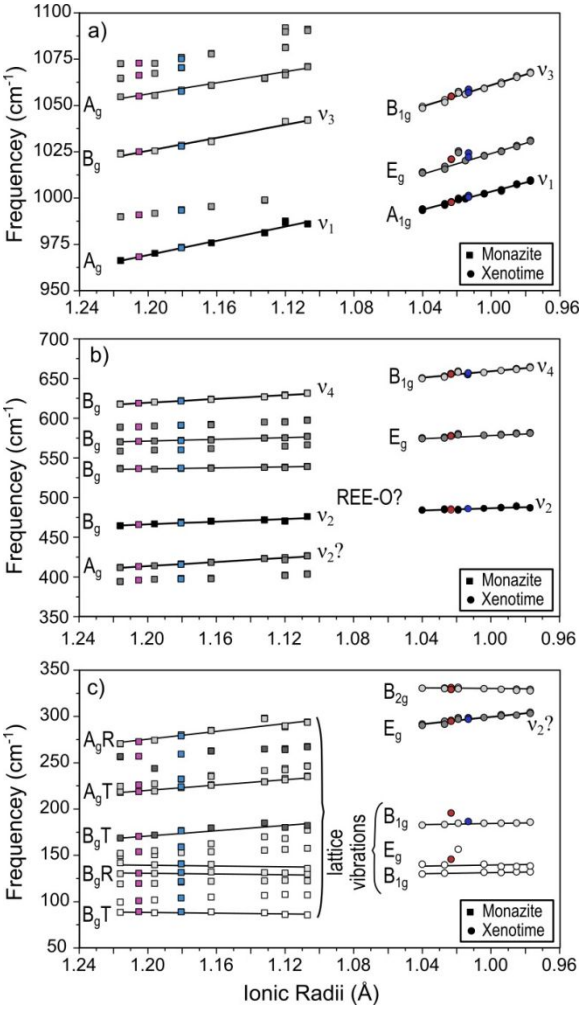

Figure 4: Trends observed for different vibrational modes with decreasing ionic radii (Shannon, 1970) in monazite between the La and Gd endmembers and 50-50 Ce-La (pink) and Ce-Nd solid solutions (light blue), and in xenotime between the Tb and Lu endmembers and 50-50 Y-Dy (red) and Y-Er solid solutions (dark blue). a) Symmetric stretching vibrational modes ν_1 and ν_3 of the PO_4 tetrahedron. b) Asymmetric stretching modes ν_2 and ν_4 of the PO_4 tetrahedron and potential mode for REE-O. c) Lattice vibrations for monazite and xenotime.

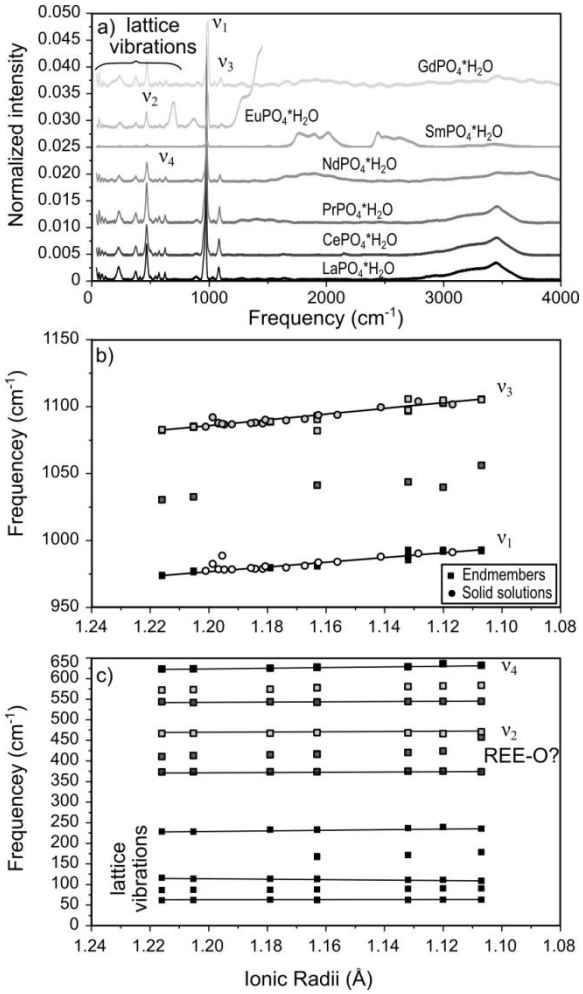

Figure 5: a) Raman spectra of rhabdophane using the 532 nm excitation laser and (B-D) corresponding peak shifts with increasing ionic radii. b) Peak centers for solid solutions shift linearly between endmembers. c) The predicted peak location for REE-O overlaps with the symmetric bending vibrational mode (ν_2).

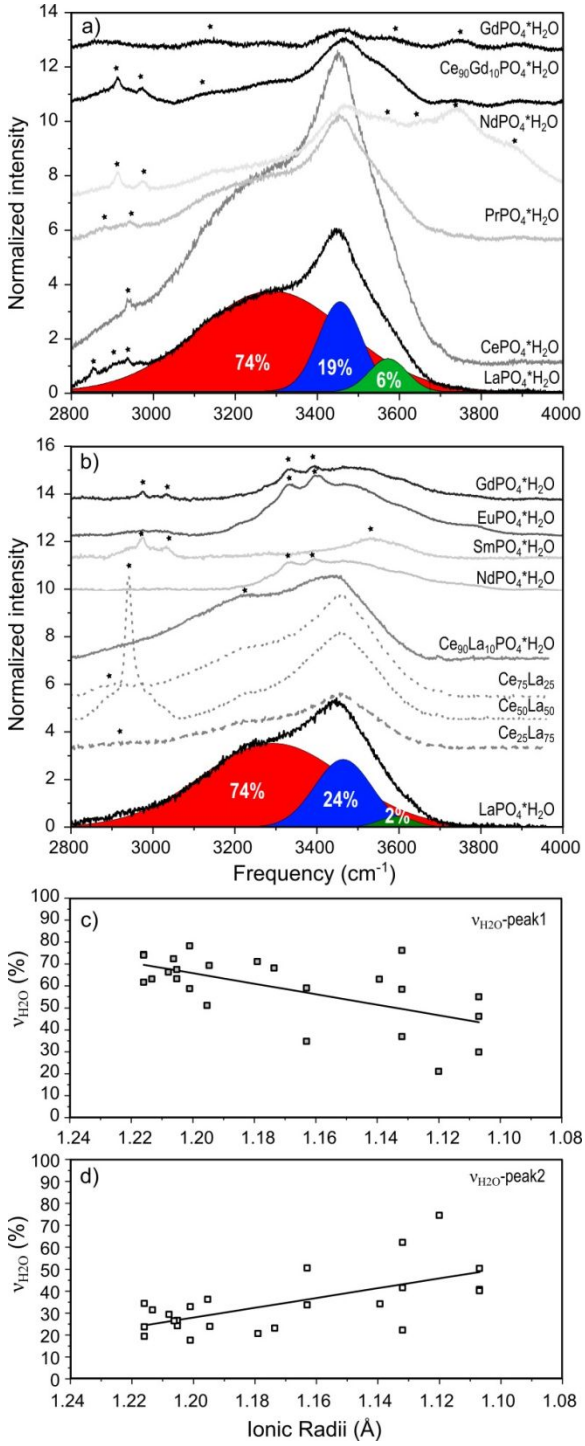

Figure 6: Raman spectra of rhabdophane endmembers and solid solutions in the region 2800 to 4000 cm^{-1} measured using the (a) 532 nm and the (b) 633 nm excitation lasers. Water peaks are deconvoluted using three peaks at ~3290, 3449 and 3596 cm^{-1}. c-d) Peak 1 (red) decreases and peak 2 (blue) increases with decreasing ionic radii between La and Gd endmembers. Photoluminescence peaks are marked with a black star.

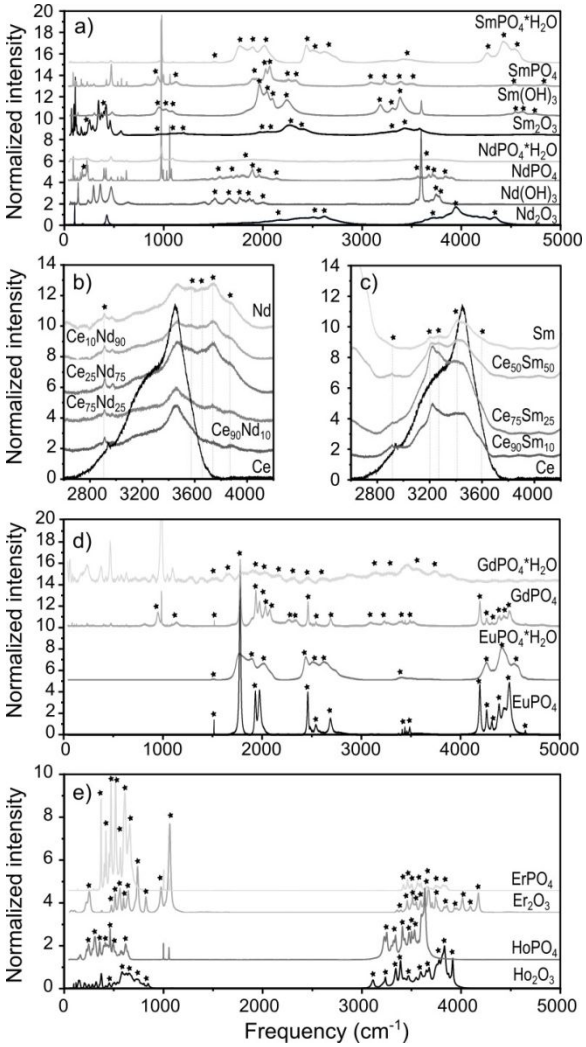

Figure 7: Photoluminescence of (a) Nd and Sm oxides, hydroxides, monazite and rhabdophane. b-c) Nd-Ce and Sm-Ce rhabdophane solid solutions overlapping with the water vibrational mode. d) Eu and Gd monazite and rhabdophane and (E) Ho and Er oxides and xenotime using the 532 nm excitation laser. Photoluminescence peaks are marked with a black star.

Tables:

Table 1: Measured Raman modes for La and Nd sesquioxides in the A-type hexagonal structure using 532 nm and the 266 nm excitation lasers.

(1)	**(2)**	**La**	**La**	**Nd**	**Nd**
		532	266	532	266
ν_2E_g		64		64	
ν_2A_g	ν_4E_g	105		103	
	ν_2A_g	191		184	
		192			229
		288			259
		364	304		
ν_1A_g	ν_1A_g	408	404	428	432
ν_1E_g	ν_3E_g				477

(1) Denning and Ross (1972), (2) Boldish and White (1979).

Table 2: Measured Raman modes for Nd, Eu, Sm and Gd sesquioxides in the B-type monoclinic structure using 532, 514.5 and 266 nm excitation lasers.

(1)	**Nd**	**Eu**	**Sm**	**Sm**	**Gd**
	(2)	(1)	(3)	(3)	(4)
		532	532	266	514.5
A_g^1		81	81		
B_g^1		96	96		
A_g^2		109	109		102
B_g^2		120	118		
A_g^3		154	169		
A_g^4		174	174		176
A_g^5		217	200		
A_g^6		244	249		
A_g^7		257	257	254	256
B_g^3		283	285	282	269
A_g^8	296	373	343	338	386
B_g^4	362	393	374	372	417
B_g^5		411	397	397	430
A_g^9	387	423	422	418	442
A_g^{10}		463	461	459	483
A_g^{11}	472	577	570	567	

(1) Candela et al. (2022), (2) Cui and Hope (2015), (3) This study, (4) Laversenne et al. (2001).

Table 3: Measured Raman modes for sesquioxide in the C-type bixbyite structure using the 532 and the 266 nm excitation lasers.

(1-2)	**(3)**	**Eu**	**Eu**	**Eu**	**Dy**	**Dy**	**Ho**	**Ho**	**Y**	**Y**	**Er**	**Er**	**Yb**	**Yb**	**Lu**	**Lu**
		532	266	266	532	266	532	266	532	266	532	266	266	266	532	266
	F_g	94			95		96				73				97	
F_g											103					
F_g+A_g	A_g	119			119		119		130						119	
	F_g	135			135				162						135	
	E_g	145			145		145		195						145	
F_g+E_g	F_g				176				273		223	269			175	
E_g	E_g+F_g	285		283	264	264			318		254	302	301	300	180	
		314	315		327	326	321	328	330	328		332	335	335	347	345
						349	357		351	353		357				370
F_g+A_g	F_g	339	333	333	372	370	374	375	377	375	378	377	360	360	392	390
		386	399	394					415			399			400	
F_g	A_g	411			424	424			431				418		453	
F_g	F_g	425			463	461		468	469	467		474	468	468	498	497
						522		526	533	528		532			555	544
					567	561		568	564	566		573	581	582	568	590
F_g	F_g	569	547	564	584	583		588	590	591		593	610	610	610	611
		637		650	592	596	644	662	643						641	

(1) Repelin et al. (1995), (2) Schaak and Koningstein (1970), (3) Abrashev et al. (2014).

Table 4: Measured Raman modes for REE hydroxides using the 532 and the 266 nm excitation lasers.

(1)	**(2-3)**	**La** 532	**La** 266	**Nd** 532	**Nd** 266	**Sm** 532	**Sm** 266	**Dy** 532	**Dy** 266	**Y** 532	**Y** 266
				44				44			
				49				49			
				51				52			
		60		60		60		60		60	
		63		64							
		67		68		67		68		67	
		71		72		72		72		71	
		75		76		75		76		75	
		83		83		83		83		83	
		91		92		91		92		91	
		94		95		94		95		94	
		99		100		99		99		99	
		107		107		107		107		107	
		111		115		115		115		115	
		117		118		117				117	
		123		123		123		123		123	
								133		129	
$E_{2g}T$		139		138		137				139	
		228	228	240	237	247		262		260	
A_g	A_{1g}	283	281	294	294	302	298	314	311	314	313
A_g	E_{2g}	341	340	362	362	376	373	395	392	399	398
A_g								406	405	406	405
E_{1g}	E_{1g}	450	451	472	469	480	482	502	499	507	506
			636	638	668	665	689	697	692	702	700
		653	654	682	686	704	703	736	732	746	746
E_{1g}			748		748		750				
			782		786		788				
			812		818		819				
		1071	1068	1073	1076		1073	1077	1079	1084	
ν_{OH}	ν_{OH}	3602	3602	3595	3598	3597	3596	3597	3598	3603	3604
						3608		3611	3612	3617	3618

(1) Arunachalam et al. (2018), (2) Liu et al. 2013, (3) Sanivarapu et al. (2018).

Table 5: Measured Raman spectra for REE xenotime endmembers and 50-50 Y-Dy and Y-Er 50-50 solid solutions using the 532 nm and the 266 nm excitation lasers.

(1-3)	(4-5)	Tb	Tb	Dy	Dy	YDy	YDy	Ho	Ho	Y	Y	YEr	YEr	Er	Er	Tm	Tm	Yb	Yb	Lu	Lu
		532	266	532	266	532	266	532	266	532	266	532	266	532	266	532	266	532	266	532	266
E_g	$B_{1g}T$	130		131										132		131		132		132	
B_g	E_gT	140		140		146				156				140		138		138		138	
E_g	$B_{1g}T$	182		183		196				185		186		184		185		185		186	
	E_gT									210		236		237			219				
E_gR	E_gR	292	290	295	291	296	295			298	297	298	297	299	299	302	300	301		304	303
B_{2g}	B_{2g}	330		330	330	331	329			331	330			330		329		329	328	329	327
A_{1g}	$A_{1g}(\nu_2)$	484	484	486	484	486	484		486	485	484		486		486	487	487	490	488	487	486
E_g	E_g	575	574	576	575	578	577			580	579				578	579	578	581	580	582	581
B_{1g}	$B_{1g}(\nu_4)$	651	650	653	652	656	655		655	659	658		657		657	660		662	661	664	663
		973	972		974	978	978				981		980		981		981		985		
A_{1g}	$A_{1g}(\nu_1)$	994	993	997	996	998	998	1000	999	1000	999	1001	1000	1002	1002	1004	1004	1008	1007	1010	1009
E_g	E_g	1014	1013	1017	1016	1021	1021	1020	1020	1025	1024	1024	1022	1023	1023	1025	1025	1028	1028	1031	1031
B_{1g}	$B_{1g}(\nu_3)$	1049	1048	1053	1052	1055	1055	1056	1056	1057	1057	1059	1057	1059	1059	1062	1062	1066	1065	1068	1067

(1) Stavrou et al. (2008), (2) Tatsi et al. (2008), (3) Dawson et al. (1971), (4) Begun et al. (1981), (5) Giarola et al. (2011).

Table 6: Measured Raman spectra for REE monazite endmembers and 50-50 Ce-La and Ce-Nd solid solutions using the 532 and the 266 nm excitation lasers.

(1)	(2)	(3)	La 532	La 266	La-Ce 532	Ce 532	Pr 532	Ce-Nd 532	Nd 532	Nd 266	Sm 532	Sm 266	Eu 532	Eu 266	Gd 532	Gd 266
B_gT	B_g	B_g	88		89	88	89	89	89		88		86		86	
A_gT	A_g	A_g	99		101	102	104		105		107		108		107	
A_gT	A_g/B_g		119		120	120	122	121	122		122		123		122	
B_gR	B_g		130		131	130	132	132	132		131		131		130	
B_gT			142			140	141	141	140						136	
A_gR	B_g/A_g	A_g	150			151		153	154		155		156		158	
A_gR		B_g	152		154	155	159	159	162		170		168		177	
B_gT	B_g/A_g	B_g	169		170	172	176	177	180		185		180		182	
B_gR		A_g	182		179										190	
A_gT	B_g	A_g/B_g	218	219	219	219	224	223	226	226	230	229	233	231	236	235
B_gR	B_g	A_g/B_g	225	225	226	227	232	232	236	235	242		244	242	247	246
A_gT	A_g	A_g	256	257	257	244	259		263	263	265	265	265	264	267	267
A_gR	A_g	A_g	270	270	273	274	279	280	285	285	298	297	289	290	294	293
$B_g\nu_2$	B_g	A_g/B_g	394	394	396	397	397	398	398	397			402	402	404	403
$A_g\nu_2$	A_g	A_g/B_g	412	412	413	414	416	416	419	418	423	423	424	421	427	426
$B_g\nu_2$	$A_g\nu_2$	$A_g/B_g\nu_2$	465	464	466	467	468	469	470	470	472	472	471	470	476	476
$B_g\nu_4$	$A_g\nu_4$		537	536	536	536	537	536	537	537	538	538	538	538	539	539
$A_g\nu_4$	$A_g\nu_4$		558			560	560		562				565	565	566	566
$B_g\nu_4$			570	570	571	571	572	572	573	572	575	575	575	575	577	577
$A_g\nu_4$	$B_g\nu_4$		588	589	589	590	591	591	592	591	595		595	595	598	597
$B_g\nu_4$	$A_g/B_g\nu_4$	$A_g/B_g\nu_4$	618	617	619	620	621	622	624	623	627	627	629	628	632	631
$A_g\nu_3$	$A_g\nu_1$	$A_g/B_g\nu_1$	966	966	968	970	973	973	976	976	981	981	988	987	986	986
$A_g\nu_3$	$A_g\nu_3$		990	990	991	992	993	994	995	995	999	999				
$B_g\nu_3$	$B_g\nu_3$		1024	1024	1025	1025	1028	1029	1031	1030			1041		1042	1042
$A_g\nu_3$	$A_g\nu_3$	$A_g/B_g\nu_3$	1055	1055	1055	1055	1058	1058	1061	1061	1064	1065	1068	1066	1071	1071
$B_g\nu_3$			1065	1065	1066	1067	1070	1070	1077	1078			1081	1081		
$B_g\nu_3$	$B_g\nu_3$		1072	1073	1073	1073	1075	1076					1092	1090	1091	1090

(1) Errandonea et al. (2018), (2) Begun et al. (1981), (3) Silva et al. (2006)

Table 7: Measured Raman spectra for REE rhabdophane endmembers using the 532 nm excitation laser.

(1)	**(2)**	**La**	**Ce**	**Pr**	**Nd**	**Sm**	**Eu**	**Gd**
		532	532	532	532	532	532	532
lattice		62	62	63	62	63	63	63
lattice		86	87	87	88	89	90	91
lattice		116	114	114	114	111	111	109
lattice					168	171		178
lattice	lattice	229	228	233	233	237	239	236
lattice	ν_2	373	374	374	373	375	375	373
ν_2	ν_2	410	413	415	417	420	424	458
	ν_2	467	467	467	469	468	466	470
		498	498	497	500	498		
ν_4	ν_4	544	541	544	543	544	544	545
ν_4	ν_4	572	573	574	578	580	582	584
ν_4	ν_4	623	624	625	628	629	636	632
ν_1		954	950	952	955	951	975	971
ν_1		970	971	975	977	976	988	987
ν_1-main	ν_1	973	976	979	981	985	992	992
ν_3	ν_3	1030	1033		1041	1044	1040	1056
ν_3-main	ν_3	1082	1084	1088	1092	1096	1106	1102
ν_{H2O}-1		3279	3280	3279	3279	3279	3321	3279
ν_{H2O}-2		3456	3457	3461	3466	3466	3485	3461
ν_{H2O}-3		3574	3573	3574	3574	3574	3587	3570

(1) Clavier et al. 2018; (2) Colomer et al. (2017)

Table 8: Symmetric and asymmetric stretching vibrational modes for rhabdophane solid solutions measured using 532 nm and the 266 nm excitation lasers.

Rhabdophane	**laser**	**grating**		**ν_1**	**ν_1**	**ν_1-main**	**ν_3**	**ν_3-main**
La	532	1800	897	964	971	974	1030	1082
La	266	2400	894	954	970	974	1031	1083
Ce	532	1800	898	962	974	977		1085
Pr25Ce75	532	1800	901	968	976	978	1034	1087
Pr50Ce50	532	1800	901	970	976	979	1039	1087
Pr75Ce25	532	1800	898	958	976	979	1034	1088
Pr90Ce10	532	1800	897	959	976	979	1035	1088
Pr	532	1800	898	963	977	980	1039	1089
Pr	266	2400	896	955	976	980	1035	1089
Nd10Ce90	532	1800	897	961	975	978		1087
Nd25Ce75	532	1800	895	972	976	979	1065	1088
Nd50Ce50	532	1800	896	972	978	980		1090
Nd75Ce25	532	1800	895	975	979	981		1091
Nd90Ce10	532	1800	896		977	982		1092
Nd	532	1800	892	975	982	982		1093
Nd	266	2400		954	984	992		1090
Sm	532	1800	895	975	984	988	1048	1097
Sm	266	2400	794		958	960	1035	
Eu10Ce90	532	1800	898	957	975	978		1087
Eu50Ce50	532	1800	893	957	979	984		1094
Eu75Ce50	532	1800	878	964	984	988		1099
Eu90Ce10	532	1800	873	967	987	990		1104
Eu	532	1800	871	979	990	993	1074	1105
Eu	266	2400		947	965		1047	
Gd10Ce90	532	1800	893	973	981	989	1062	1087
Gd25Ce75	532	1800	898	973	978	981		1090
Gd50Ce50	532	1800	904	975	982	984	1039	1094
Gd90Ce10	532	1800	900	975	988	991	1050	1102
Gd	532	1800	904	985	991	993	1044	1105

Table 9: Water peak centers, full width half maxima (FWHM) and area % for rhabdophane endmembers and solid solutions using 266, 532 and 633 nm excitation lasers.

Compound	Laser	Grating	Center			FWHM			Area%		
			1	2	3	1	2	3	1	2	3
Free Water	532	1800	3279	3446	3581	315	140	154	69	18	13
La	532	600	3289	3455	3572	429	126	110	74	19	6
La	633	600	3293	3464	3595	414	164	101	74	24	2
La	266	2400	3420	3465	3563	267	130	67	62	34	4
Ce10La90	633	600	3222	3418	3535	185	172	107			
Ce25La75	633	600	3296	3464	3576	364	149	111	63	31	5
Ce50La50	633	600	3246	3457	3620	176	205	135			
Ce75La25	633	600	3302	3467	3582	399	150	118	66	29	4
Ce90La10	633	600	3243	3450	3558	403	176	82	72	26	1
Ce	532	600	3272	3458	3577	387	140	132	67	24	8
Ce	266	2400	3338	3459	3566	380	122	117	63	27	10
Pr	532	600	3306	3457	3562	433	116	116	71	21	8
Nd10Ce90	532	600	3379	3459	3559	548	110	84	78	18	4
Nd25Ce75	532	600	3302	3457	3559	453	113	84	69	24	7
Ce50Nd50	532	600	3277	3471	3608	446	177	190	59	33	8
Nd75Ce25	532	600	3360	3466	3568	453	113	84	68	23	9
Nd	532	600	3302	3480	3574	460	164	74	59	34	7
Nd	633	600	3334	3434	3568	104	242	347			
Sm50Ce50	532	600	3105	3222	3427	79	146	266			
Sm75Ce25	532	600	3227	3252	3452	136	424	254			
Sm90Ce10	532	600	3243	3466	3595	261	181	72	63	34	3
Sm	532	600	3232	3428	3512	144	149	288			
Sm	266	2400	3346	3432		745	215		58	42	0
Sm	633	600	3380	3545	3617	319	162	35	37	62	1
Eu	532	600	3394	3470	3658	65	152	181			
Eu	633	600	3349	3481	3776	176	317	150	21	75	4
Gd	532	600	3187	3460	3573	308	112	76	46	41	13
Gd	532	600	3199	3459	3572	243	107	83	30	50	20
Gd	266	2400	3345	3491	3744	208	163	34	55	40	5
Gd	633	600	3339	3478	3774	96	305	69			